Applied Surface Science 690 (2025) 162576

Contents lists available at ScienceDirect

Applied Surface Science

journal homepage: www.elsevier.com/locate/apsusc

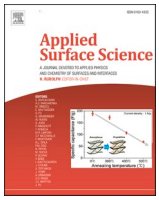

Full Length Article

Evaluation of iron oxide coatings as electrocatalysts for oxygen evolution reaction obtained via electrodeposition and magnetron sputtering

Ieva Barauskienė [a,*], Jean-François Blach [b], Sebastien Saitzek [b], Jolanta Rousseau [b], Christian Mathieu [b], Vidas Pakštas [c], Eugenijus Valatka [d], Giedrius Laukaitis [a]

[a] Department of Physics, Faculty of Mathematics and Natural Sciences, Kaunas University of Technology, Studentų str. 50, 51368 Kaunas, Lithuania
[b] Univ. Artois, CNRS, Centrale Lille, Univ. Lille, UMR 8181, Unité de Catalyse et Chimie du Solide (UCCS), F-62300 Lens, France
[c] Center for Physical Sciences & Technology, Saulėtekio al. 3, 10257 Vilnius, Lithuania
[d] Department of Physical and Inorganic Chemistry, Faculty of Chemical Technology, Kaunas University of Technology, Radvilėnų str. 19, 50254 Kaunas, Lithuania

ARTICLE INFO

Keywords:
Oxygen evolution reaction
Water splitting
Magnetron sputtering
Electrodeposition

ABSTRACT

In this work, the electrocatalytic activity of hematite with a porous and compact structure was investigated in the process of oxygen evolution. Porous coatings were synthesized using potentiodynamic ElectroDeposition (ED) and thermal treatment, while compact coatings were synthesized by Magnetron Sputtering (MS). Electrocatalytic evaluation of the coatings showed that there is no significant difference with respect to the overpotential of the reaction onset potential, which is 342–353 mV for electrodeposited samples and 341–355 mV for those obtained by the MS method. However, the advantage of compact coatings has emerged at higher current density values, when the activity of porous coatings faces limitations due to diffusion from and into the pores. Calculations of the coefficient *b* of the Tafel equation revealed the superiority of porous structures (avg. 48 mV·dec^{-1}) at the beginning of the reaction over compact coatings (avg. 56 mV·dec^{-1}).

1. Introduction

The United Nations' (UN) goal of reaching carbon neutrality by 2050 heavily relies on using renewable energy sources [1,2]. However, certain carbon-intensive industries, like steel, chemicals, and transport, cannot be fully decarbonized through electrification alone and need more intricate solutions. Hydrogen, with its high energy density, has the potential to serve as the crucial element in the energy transition [3]. Hydrogen can be utilized as a feedstock, fuel, or energy carrier and storage medium. However, fossil fuels, particularly natural gas and coal, remain the primary raw materials for hydrogen production, leading to the emission of 70 to 100 million tons of CO_2 annually in the EU. When produced from renewable sources through water electrolysis, hydrogen has the potential to revolutionize the global energy economy [4].

The two main industrial electrolysis technologies, Alkaline Electrolysis (AE) and Proton Exchange Membrane (PEM) electrolysis, do not offer a clear economic advantage over traditional hydrogen production methods. AE uses inexpensive nickel electrodes but faces issues related to safety of operation (6 M KOH), low efficiency (65–68 percent), and sensitivity to power grid fluctuations when using renewable sources. PEM is efficient but depends on scarce and expensive elements like iridium (Ir) and platinum (Pt) [5] for electrocatalysts, and the production of PEM membranes releases ozone-depleting fluorocarbons [6]. Anion-Exchange Membrane (AEM) electrolysis is an emerging technology that uses abundant and inexpensive metals or their derivatives as catalysts while maintaining high electrolyzer efficiency [4]. This alternative reduces the fabrication cost of AEM and promotes its commercialization. AEM uses much safer polymer membranes and a mild alkaline (0.1–1 M) electrolyte, which helps prevent the rapid corrosion that is a major concern in AE. However, as a relatively new technology, AEM faces numerous challenges that must be addressed to realize its full potential. The efficiency of AEM largely depends on the hydrogen evolution (HER) and oxygen evolution (OER) electrocatalysts, as their kinetics and durability are crucial for effective water splitting [5]. Although OER is favourable in alkaline conditions, it is more energy-intensive than HER due to its complex four-step reaction pathway, resulting in sluggish kinetics and typically high overpotentials [5]. Extensive research has been conducted on various materials, with significant focus on transition metals (TM) and their sulphides, phosphides, and nitrides. Recently, it was discovered that the real active species in

* Corresponding author.
E-mail address: ieva.barauskiene@ktu.lt (I. Barauskienė).

https://doi.org/10.1016/j.apsusc.2025.162576
Received 9 October 2024; Received in revised form 14 December 2024; Accepted 28 January 2025
Available online 31 January 2025

TM-based electrocatalysts are the transformed metal oxides (TMO) or (oxy)hydroxides (TM-(O)OH) [7]. Among the different spinel oxides, iron oxides have shown low overpotentials, fast kinetics, excellent long-term durability, and adaptability to different environmental conditions [8,9].

γ-Fe_2O_3 is a familiar phase of iron oxide and exists in metastable state in nature. It has a cubic crystal structure of an inversive spinel type ($P4_132$ space group with the lattice constant of $a = 8.351$ Å), in which the oxygen anions have a cubic close-packed array. Meanwhile, in α-Fe_2O_3, two-thirds of the octahedral sites are occupied by Fe(III) ions. Moreover, the special arrangement of Fe(III) ions needs to maximize the distance between them [10]. It was determined by Xu et *al.* [10] that α-phase is more advantageous in OER with the overpotential of 275 mV at 10 mA·cm^{-2} due to the presence of more Fe active sites (Fe^{3+}) exposed on the surface. These Fe active sites are beneficial to enhance the adsorption of hydroxyl groups in water molecules.

The synthesis method significantly impacts the film's morphology and porosity, which determines the electrocatalytic activity of the coatings as well. Optimized porosity enhances ion and electrolyte accessibility to active sites and increases the surface area [11]. However, compact films can help prevent undesirable side processes, such as slow diffusion, within the pores [12]. The ideal porosity and pore size distribution, particularly important for reactions generating gaseous products (OER), remain undetermined. Electrodeposition is of great interest due to its relatively easy and precise control over the surface microstructure of deposited films by adjusting variables like electrolyte composition, deposition potential, and bath temperature [13]. This low-temperature technique is straightforward to perform and requires inexpensive equipment. Meanwhile, physical vapor deposition (PVD), including magnetron sputtering, offers high purity, uniformity, and compactness of films, with easy control over composition, particle size, and crystallinity by modifying parameters. MS is highly reproducible, scalable to large areas, residue-free (unlike other methods using liquid solvents) and operates at room temperature [14]. Improving substrate parameters such as specific surface area, corrosion resistance, high conductivity and environmental friendliness makes a huge contribution to enhancing overall process efficacy [15].

The aim of this study was to compare the electrocatalytic activity of porous and compact iron oxide coatings in the oxygen evolution reactions. The coatings were produced using two energy-efficient synthesis technologies that create either porous or compact structures. Electrochemical deposition was employed to prepare porous samples, while magnetron sputtering was used to produce compact coatings.

2. Materials and methods

2.1. Synthesis

Electrochemical deposition of iron oxide coatings was performed on commercially available AISI302 type stainless steel plates (Goodfellow, Germany) using potentiodynamic cycling. The potential was swept from −1.1 V to + 1.1 V vs Ag/AgCl|$KCl_{(sat)}$ reference electrode at a scan rate of 50 mV·s^{-1}. The electrolyte used had the following composition: 0.05 M $Fe(NO_3)_3$ + 0.1 M KNO_3 (Chempur, Poland). Since the acidic nature of the synthesis solution is not favourable for the formation of hydroxide ions, the pH values were adjusted with the addition of 0.5 M KOH (Chempur, Poland), ranging from 1.28 to 1.98 with a step of 0.05. The electrodeposited coatings were annealed in air atmosphere at 400 °C for 1 h. Synthesis of compact coatings was performed via magnetron sputtering using Kurt J. Lesker PVD75 system. The pulse DC power source was fixed at 300 W and pure hematite target was used. Three different atmospheres were applied by varying the ratio of oxygen to argon: 100 % Ar, 70 % Ar/30 % O_2, and 20 % Ar/80 % O_2. No additional heating of the substrate was used.

2.2. Characterization

The phase structure of deposited coatings was analyzed with the ULTIMA IV (Rigaku) X-ray diffractometer using nickel-filtered copper $K_{\overline{\alpha}}$ radiation ($\lambda = 1.5418 \times 10^{-10}$ m), with the tension voltage and current set at 40 kV and 40 mA, respectively. XRD patterns were collected from 15 to 80° (2θ) at a step size of 0.02° and count time of 3 s by step.

Surface topography images were obtained using Hitachi SU3800 scanning electron microscope (SEM). Raman analysis was performed with Horiba Labram HR spectrometer with a NIR Laser beam (784 nm, power 2 mW) focused with a X50 microscope objective.

X-ray photoelectron spectrometer (XPS, PHI Versaprobe 5000) was used for determination of iron oxidation state and analysis of surface composition. XPS spectra were collected with monochromated 1486.6 eV Al radiation, 25 W beam power, 100 µm beam size, 45° measurement angle. Samples were sputtered with Ar for 1 min to obtain the composition of as-deposited coatings.

Electrocatalytical activity of all samples was evaluated using a potenciostat/galvanostat BioLogic SP-150 (BioLogic Science Instruments, Seyssinet-Pariset, France). A three-electrode configuration was employed, consisting of a working electrode (prepared coatings, 1 × 3 cm), a counter electrode (Pt wire, 15 cm^2), and a reference electrode (Ag,AgCl|$KCl_{(sat)}$). The EC-Lab V10.39 software was used for collection and treatment of the experimental data. Potential-controlled electrolysis was performed in 1.0 M KOH to construct the Tafel plots. The following equation was used for calculation of the overpotential [16]:

$$\eta = E_{appl} - E_{eq} \quad (1)$$

where E_{appl} is the applied potential (V) vs Ag,AgCl|KCl(sat), and E_{eq} is the equilibrium potential of the OER pH = 14.0. All electrochemical experiments were performed without *i*R compensation. During the measurements the dissolved oxygen and carbon dioxide gases were not additionally removed.

Potentiostatic Electrochemical Impedance Spectroscopy (PEIS) measurements were conducted in 1.0 M KOH, in the frequency range from 10^5 to 10^{-2} Hz with a sinus amplitude of 20 mV without *i*R compensation.

The corrosion rate of iron oxide coatings was evaluated by potentiodynamic scanning in 1.0 M KOH solution at E_{oc} ± 200 mV. The corrosion rate was calculated EC-Lab V10.39 software according to the following equation:

$$CR = \frac{I_{corr} \times K \times EW}{d \times A} \quad (2)$$

Where I_{corr} is the corrosion current (A), K – a constant (3272 mm·A^{-1}·cm^{-1}·year^{-1}), EW is the equivalent weight for Fe_2O_3 (g per equivalent), d – density (g·cm^{-3}) and A is the electrode surface area (cm^2).

All potential values were standardized according to the reversible hydrogen electrode (RHE) with the following formula:

$$E_{RHE} = E_{Ag,AgCl} + E^0_{Ag,AgCl} + 0.059 \times pH \quad (3)$$

The average crystallite size, where needed, was calculated according to Scherrer's equation [17]. For the determination of average crystallite size, the instrumental contribution was deconvoluted of XRD line profile (microsized-LaB6 was used to determine the instrumental function).

pH measurements were conducted using WTW pH 330 pH-meter with Sentix 41 probe.

3. Results and discussion

3.1. Electrochemically prepared iron oxide coatings

3.1.1. Electrochemical synthesis and influence of pH

The voltammetric behaviour of AISI 302 type stainless steel electrode in 0.05 $Fe(NO_3)_3$ with 0.1 M KNO_3 electrolyte is shown in Fig. 1. The

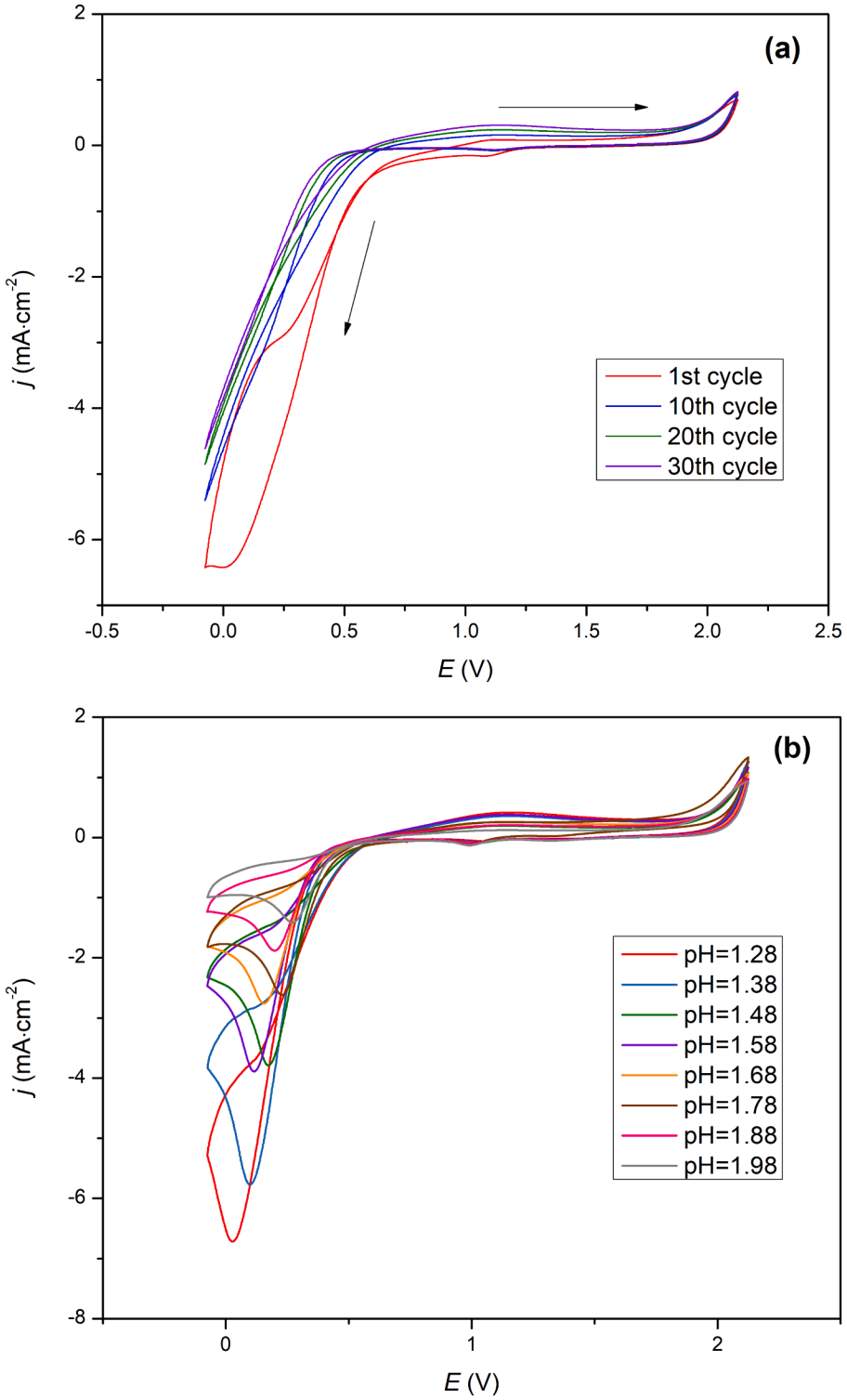

Fig. 1. Influence of the number of cycles (*a*) and pH value (*b*) to the cyclic voltammograms of AISI302 stainless steel in 0.05 M $Fe(NO_3)_3$ + 0.1 M KNO_3 electrolyte. pH values were balanced with 0.5 M KOH.

coating synthesis process consisted of 30 cycles, sweeping the potential from –0.1 V to + 2.1 V, when the nature of the curve reached a stable mechanism already during the second cycle (Fig. 1a). Sweeping negatively from an initial potential of around –0.823 V, the increase in cathodic current starts at around –0.423 V, and the maximum of the peak is reached depending on the pH value of the solution (Fig. 1b). By alkalinizing the deposition solution from the initial value (1.28) to 1.98, a shift of the cathodic peak towards more positive potentials is observed. Generally, this peak can be related to the reduction of nitrate ions and formation of hydroxy groups [18,19]:

$$NO_3^- + H_2O + 2e^- \rightarrow NO_2^- + 2OH^- \quad (4)$$

As a result of this process, the pH of the electrolyte near the electrode increases. Therefore, it is likely that at a higher pH value of the solution, a lower potential value is required for the reduction of nitrate ions. The hydroxyl groups formed via electrochemical reduction are expected to

react with Fe(III) ions present in the electrolyte. Consequently, iron hydroxide is deposited on the electrodes according to reaction:

$$Fe^{3+} + 3OH^{-} \rightarrow Fe(OH)_3 \quad (5)$$

According to the Pourbaix diagram, at pH > 2 iron ions tend to combine with hydroxide ions to form iron hydroxide precipitates. Up to this value, the solution may contain Fe^{3+}, $Fe(OH)^{2+}$ or even $Fe(OH)_2^{+}$ ions. It is likely that when the precipitation solution is alkalinized, structures with a lower oxidation state are more dominant, requiring only one or two hydroxide ions to bind to form an insoluble hydroxide. Therefore, a lower current density is required for hydroxide formation reactions to occur. The acidic environment of the solution is favourable for the hydrogen evolution reaction, so it is likely that the reduction of the nitrate ion can compete with the formation of H_2:

$$2H^{+} + 2e^{-} \rightarrow H_2 \quad (6)$$

When monitoring the quality of the substrate coating process with iron hydroxide, it was observed that the best quality coatings were obtained from the electrolyte within a pH range of 1.73–1.83. Meanwhile, at lower or higher pH values, coverage irregularities of coatings were found. These fluctuations may be related to the optimal concentration of Fe^{3+}, $Fe(OH)^{2+}$ and $Fe(OH)_2^{+}$ ions, which determines a sufficient but not too fast reaction rate of the EC mechanism (electrochemical reaction followed by an irreversible chemical reaction).

3.1.2. Structural characterization

After magnetron sputtering, it was observed that different argon-to-oxygen ratios resulted in different colour coatings, despite other chamber conditions being kept the same. Although the structural analysis of the coatings did not reveal significant differences in the phase composition of the coatings, the thickness of the coating may be a factor determining the colour. When the layer is thin, the colour is a result of interference effects. However, after reaching the saturation point, the colour of the film no longer varies with thickness, indicating that it is due to absorption effects. Magnetite (Fe_3O_4) and hematite (Fe_2O_3) has different saturation points, which are 285 nm and 1365 nm, respectively [20]. The colour transition follows the sequence with the thickness: yellow-pink-blue-grey. Deposition of the coatings under an argon-only atmosphere and when the ratio of Ar to O_2 is maintained at 20%/80 % produces pink coatings, while blue coatings are formed when the ratio in the chamber is 70 %Ar/30 %O_2.

The structural characterization of formed coatings was performed with X-ray diffraction analysis. The XRD patterns presented in Fig. 2 also includes the X-ray diffractogram of uncoated AISI302 type stainless steel. Due to the thinness of the synthesized coatings, the three base peaks are assigned to the steel substrate, two of which at $2\theta = 44.02°$ and 50.68° are associated with a face-centred cubic (δ-FCC) structure of austenite with an ICDD PDF No. 33–397 (d = 0.2075, 0.1796 nm), and the peak at $2\theta = 44.84°$ is assigned to the alloy of iron and chromium (α-Fe-Cr – body centred cubic structure) with an ICDD PDF No. 34–396 (d = 0.2035, 0.1438 nm). Meanwhile, in the spectrum of the electrodeposited and annealed coating, in addition to the base peaks, the peaks at $2\theta = 24.15°$, 33.16°, 35.96°, 38.60°, and 65.22°, which are all identified as α-Fe_2O_3 with ICDD PDF No. 33–0664, are also evident. The lack of crystallinity and amorphous structure of coatings deposited via MS under only argon atmosphere in the chamber hinder the identification, as only broadened peaks in the range of 2θ = 26-38° are obtained. Meanwhile, increasing the amount of oxygen in the chamber results in an obvious increase in crystallinity. In this case, two phases of iron oxides are highlighted. The first is a hematite structure (α-Fe_2O_3, ICDD PDF No. 33–0664) with the (012), (104), (113), (024), (116) and (018) reflections located at $2\theta = 14.16°$, 33.12°, 40.56°, 49.4°, 54.18° and 57.54°, respectively. The second is a magnetite structure (Fe_3O_4, ICDD PDF No. 19–629) with the (311) and (440) reflections located at 35.86° and 62.38°, respectively. This result confirms the previous hypothesis of the presence of these two phases in coating. In addition, the significant broadening of the diffraction peaks for the iron oxide phases indicates the presence of a layer consisting of nanometer-sized crystallite on the surface of the steel substrate.

The spectrum of Raman analysis (Fig. 3) revealed good crystallinity

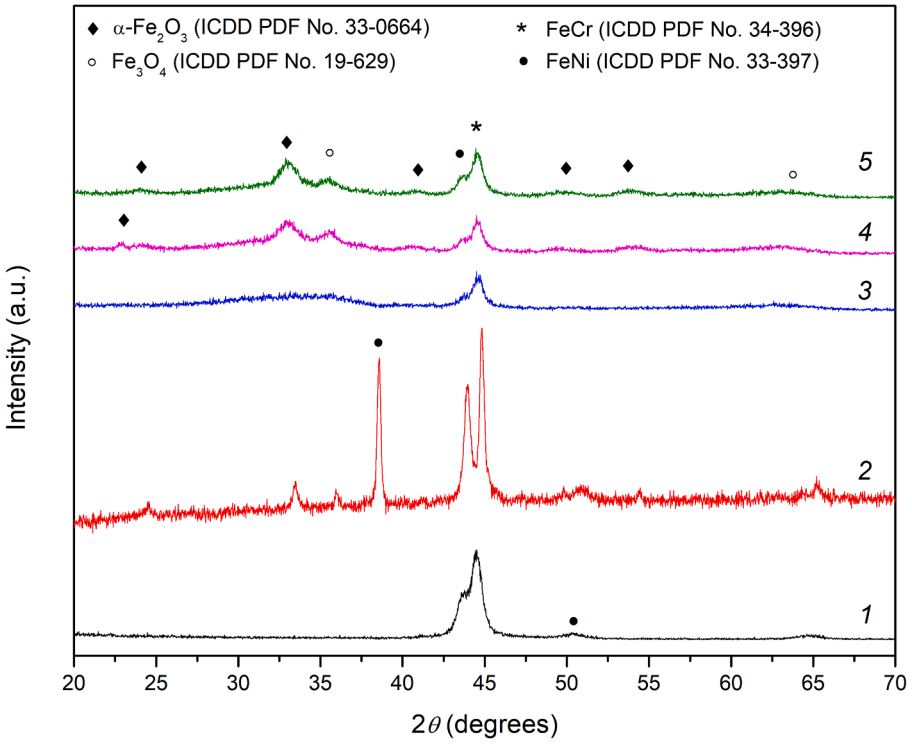

Fig. 2. XRD spectra of AISI302 base (*1*), electrodeposited and annealed iron oxide formed at pH=1.78 (*2*) and coatings, obtained by MS technique at different argon and oxygen ratios: 100% Ar (*3*), 70%Ar/30%O_2 (*4*), and 20%Ar/80%O_2 (*5*)n.

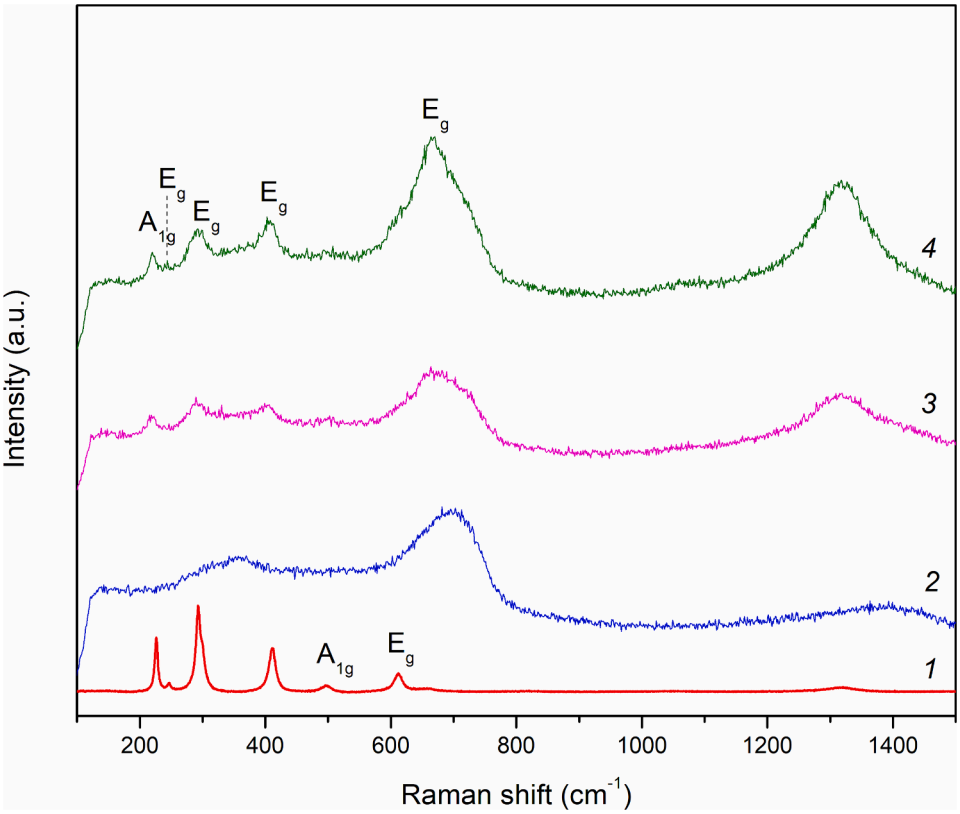

Fig. 3. Raman spectra of electrodeposited and annealed iron oxide formed at pH=1.78 (*1*), and coatings, obtained by MS technique at different argon and oxygen ratios: 100% Ar (*2*), 70%Ar/30%O_2 (*3*) and 20%Ar/80%O_2 (*4*).

of the electrodeposited coatings, as the obtained peaks are of high intensity and low width. The spectrum is composed of E_g symmetric stretching vibrations at 611, 410, 292, and 232 cm^{-1}, A_{1g} antisymmetric bonding vibrations at 495 and 226 cm^{-1}, and a broaden peak with a maximum at 1315 cm^{-1}. All these peaks agree well with a spectrum of a hematite [21]. Raman analysis of iron oxide synthesized by magnetron sputtering confirms XRD results that the coatings are more amorphous than electrochemically deposited and annealed hematite as we can note a broadening of Raman lines. In addition to the synthesis method, the ratio of argon to oxygen also affects the crystallinity. This is also reflected in the Raman spectra of the samples. In the spectra of the samples formed in a 100 % argon atmosphere, only three faded peaks are recorded. Although hematite peaks at around 1300 and 660 cm^{-1} are common to all samples, a higher oxygen content directly increases the crystallinity of the coatings. This is confirmed by the pronounced peaks at 400 and 289 cm^{-1} related to symmetric stretching vibrations followed by the antisymmetric bonding vibrations at 221 cm^{-1} in the spectra of the argon and oxygen mixture [22].

Morphological studies of electrodeposited and annealed α-Fe_2O_3 shows a distinctive clustering behaviour at lower magnification (Fig. 4a andb), while at higher magnification horizontally oriented lamellar structure can be seen (Fig. 4c). It was estimated that the diameter of the formed clusters ranges from 240 nm to 310 nm. Unlike electrochemically deposited and annealed coatings, magnetron sputtering allowed for the formation of much more compact coatings. SEM images (Fig. 4 d-f) confirm the thinness of the coatings, as a surface is obtained that replicates the steel substrate without covering its irregularities. Although the compactness of the surface is clearly visible, agglomerates of coating growth within the range of 200–600 nm are also observed. Basically, the same morphology is characteristic of all MS-formed coatings, regardless of the ratio of argon to oxygen.

3.1.3. *Electrochemical activity in OER*

The catalytic evaluation of the prepared hematite on AISI302 stainless steel samples began with the examination of their ability to promote oxygen formation. Steady state linear sweep voltammograms (LSV) of coatings prepared by electrochemical deposition and magnetron sputtering were recorded in 1.0 M KOH and are displayed in Fig. 5. According to the generally assumed OER mechanism at alkaline conditions, four electrons are released to produce and oxygen molecule [3]. Starting with an adsorption of OH^- ion on the active sites of hematite which should be already transformed to a monolayer of (oxy) hydroxide right after immersion [7], the first electron is released. The real active area and hydrophilicity are the key factors in this step; therefore, a porous structure is highly encouraged. For the calculations of electrochemically active surface (ECSA), cyclic voltammograms were recorded in non-faradaic region for all the coatings in the potential range $E_{oc} \pm 100$ mV (Fig. S1). According to the results in Table 2, the ECSA of electrodeposited sample differs significantly from iron oxide formed by MS and is the lowest among the tested coatings. Although the absolute values of ECSA should be considered critically [23], the recorded CV curves clearly emphasize that the porous coating deposited by the ED has a lower double layer capacity, possibly due to the more difficult access of ions to the pores of the coating.

The next step in the four-electron process is the oxidation of the surface hydroxyl species to oxide, producing an electron and a pair of protons. The complexity of the OER mechanism places high demands on the catalyst surface, namely a sufficient concentration of active centres and an optimal binding energy of intermediate OER derivatives. The further course of the process, regardless of whether it takes place in the case of further oxidation of the catalyst monolayer to oxyhydroxide or in the connection of adjacent oxo species, depends greatly on the binding energy and the conductivity of the catalyst.

Considering the catalytic activity of the hematite coatings prepared by electrodeposition, the intense rise of the anodic current at of 20

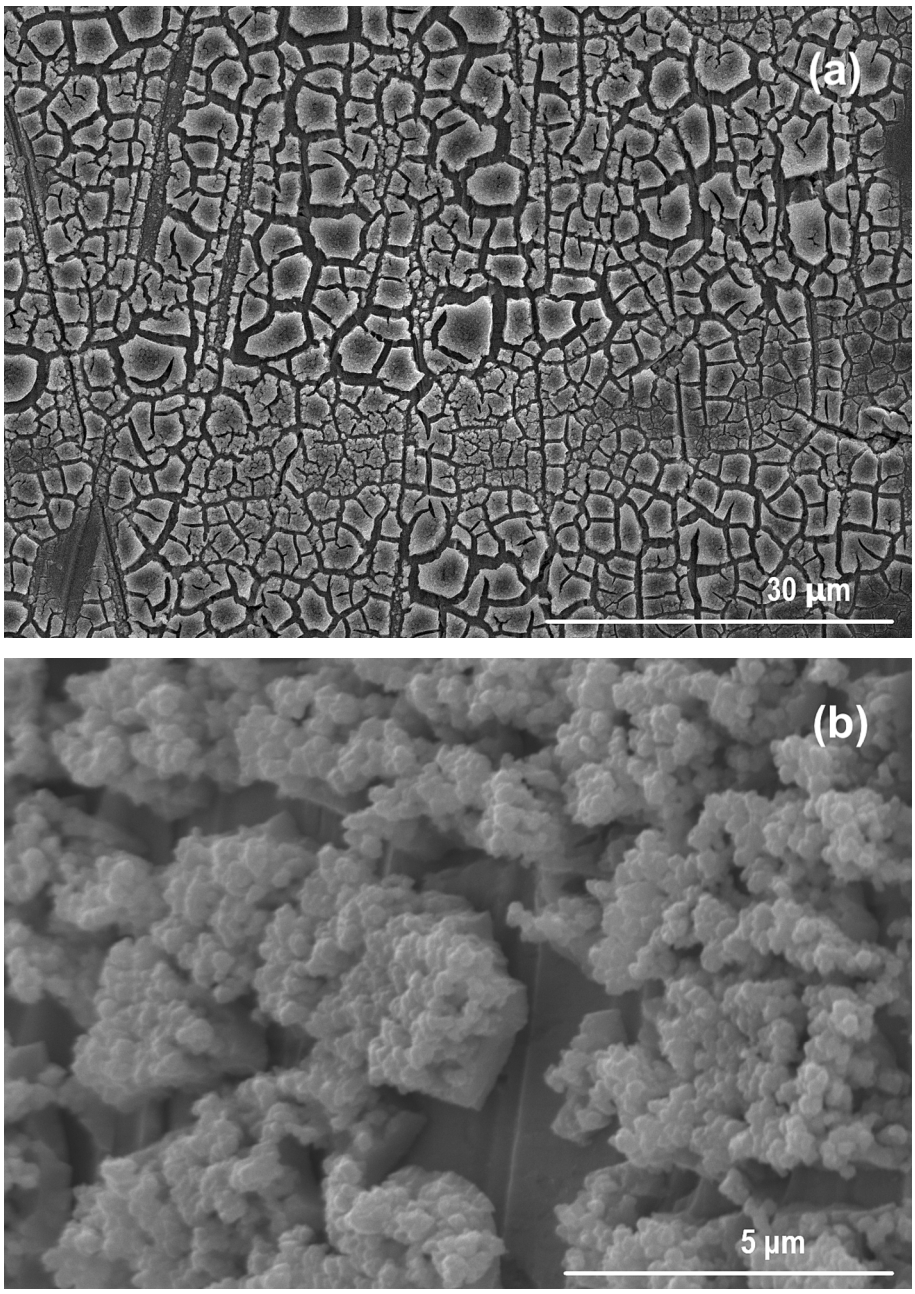

Fig. 4. SEM micrographs of iron oxide prepared by ED (*a-c*) and MS (*d-f*) techniques at different Ar and O_2 ratios (*d* - 100% Ar, *e* - 70%Ar/30%O_2, *f* - 20%Ar/80%O_2) and different magnifications: *a* - ×1600, *b* - ×9000, *c* - ×27000, *d* - ×2000.

$mV \cdot s^{-1}$ (Fig. 5a) is recorded only at potential values higher than 1.52 V. However, at higher current densities, a pair of redox reactions emerges in the potential range of 1.37–1.57 V (Fig. S2a). These reactions are likely to be related to Fe(II)/Fe(III) redox reactions, which suggest the possibility of a small amount of magnetite (Fe_3O_4) in the coating though XRD analysis suggests differently. After conducting multiple scanning in the anodic region (Fig. S3), no redox peak in the Fe(II)/Fe(III) transition potential range was detected during first scans but was a result of multiple scanning. It can signify about the slow formation of magnetite during oxygen generation. As illustrated in Fig. S2b, which was composed according to the results of Fig. S2a, the faster scanning speed resulted in a linear increase in the anodic and cathodic peak heights within the potential range of 1.37–1.57 V, without altering the current density values during the OER. Typically, any deviation from this linear behaviour can be attributed to internal capacitance, which arises due to the slow penetration of hydroxide ions into less accessible regions, such as micropores, cracks, and corners, as well as the sluggish electron transfer [24].

Structure studies have revealed that the coatings formed by the magnetron sputtering method have the same prevailing hematite structure as the electrochemically deposited ones. Therefore, it is not surprising that electrocatalytic activity measurements displayed very similar behaviour in the 1.0–1.5 V potential range (Fig. 5b). However, the situation changes when the process of oxygen evolution intensifies, as well as the formation of bubbles. The compact structure then demonstrates its advantage, as the pores of the porous structure no longer block the path of the formed oxygen bubbles, and they are more easily removed from the catalyst surface [12]. However, at higher potentials, the current densities of these coatings are also partially limited by diffusion, since the tilt angle of the *j-E* curve along the x axis decreases.

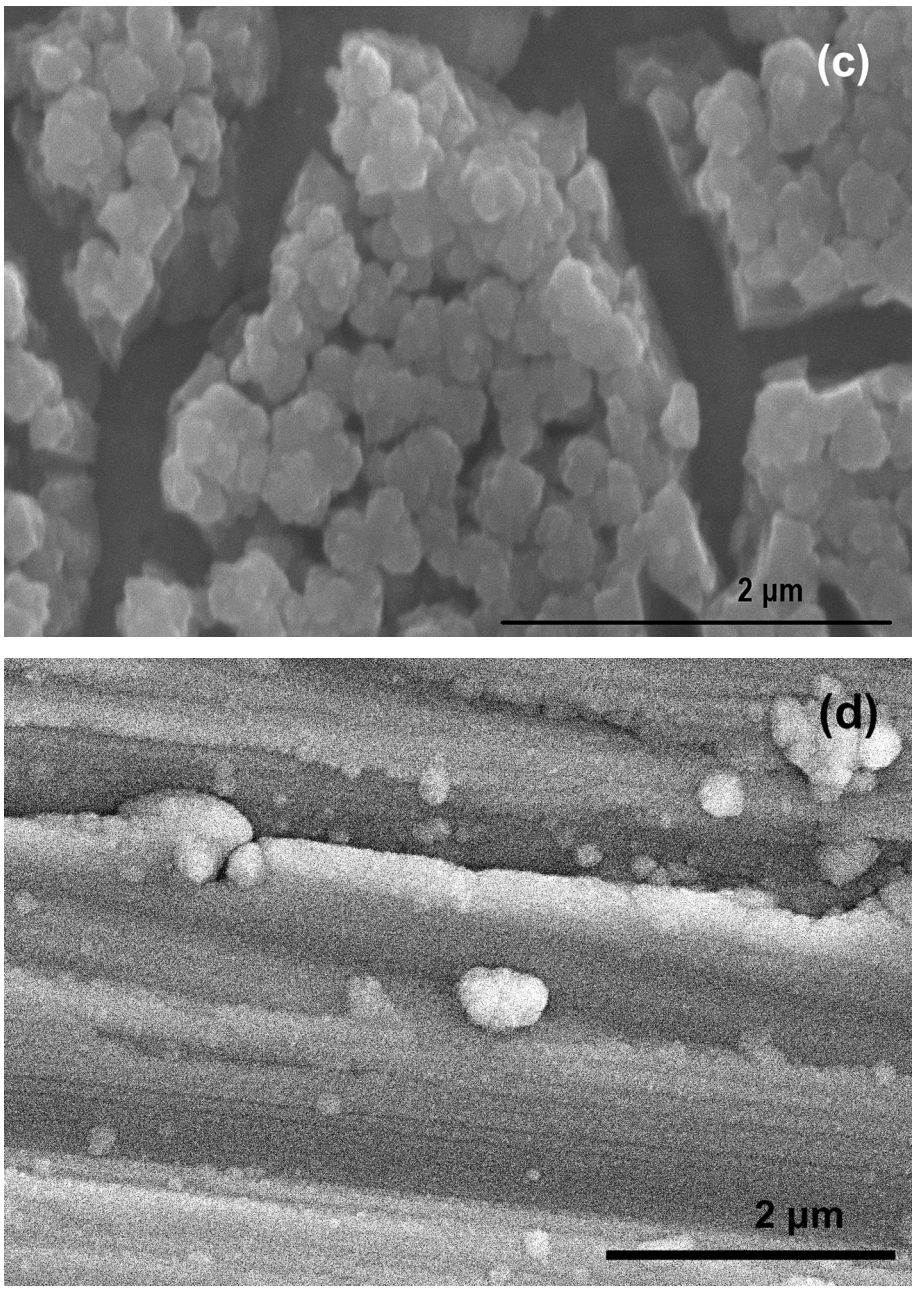

Fig. 4. (*continued*).

The same pair of redox peaks at 1.32–1.52 V remains in the case of these coatings, but unlike the porous ones, these peaks are slightly less intense in terms of current density. Since these peaks are likely related to the Fe (II)/Fe(III) transformation, their lower intensity suggests that the MS-deposited coatings might be purer hematite structures.

Comparing the results of the catalytic activity studies of coatings deposited with different chamber gas compositions, LSV measurements did not highlight a clear advantage of the amorphous coatings over crystalline ones. However, after conducting a staircase chronopotentiometry as a part of testing protocol of electrocatalysts [25] (Fig. S4), it was noted that amorphous iron oxide possessed lower potential values at higher current densities as well as the smoother and more stable signal in CPs. Since XRD and Raman analysis did not identify clear differences between coatings deposited via magnetron sputtering, XPS analysis was conducted for amorphous (100 % Ar) and crystalline (70 %Ar/30 %O_2) coatings (Fig. 6 and Fig. S5). Results indicated that both coatings have oxyhydroxide species on the surface that disappears after the sputtering procedure for 1 min. The Fe2p (Fig. 6a) and O1s (Fig. 6b) spectra of sputtered coatings present typical peaks of Fe^{2+} at 709.05 eV (Fe2p) and 529.9 eV (O1s), and Fe^{3+} at 710.91 eV (Fe2p) and 530.1 eV (O1s). According to the calculations of FeO and Fe_2O_3 amounts in the composition of examined samples, amorphous coating has 17 % of Fe(II) and 83 % of Fe(III) while introduction of oxygen gas in the deposition chamber increases the content of Fe(II) to 28 % with only 72 % of Fe(III).

Although the XRD and Raman analysis did not reveal clear differences between the coatings deposited with 30 % and 80 % oxygen, and the average calculated crystallite size is relatively the same (6.2 and 5.7 $\pm$ 2 nm, respectively), the differences in the activity of the coatings can be associated with a higher number of active sites that amorphous structures usually present.

The kinetic parameters of the electrocatalytic activity of the coatings are presented in Table 1. The data signify that the pH value of the solution during electrochemical deposition does not have a significant

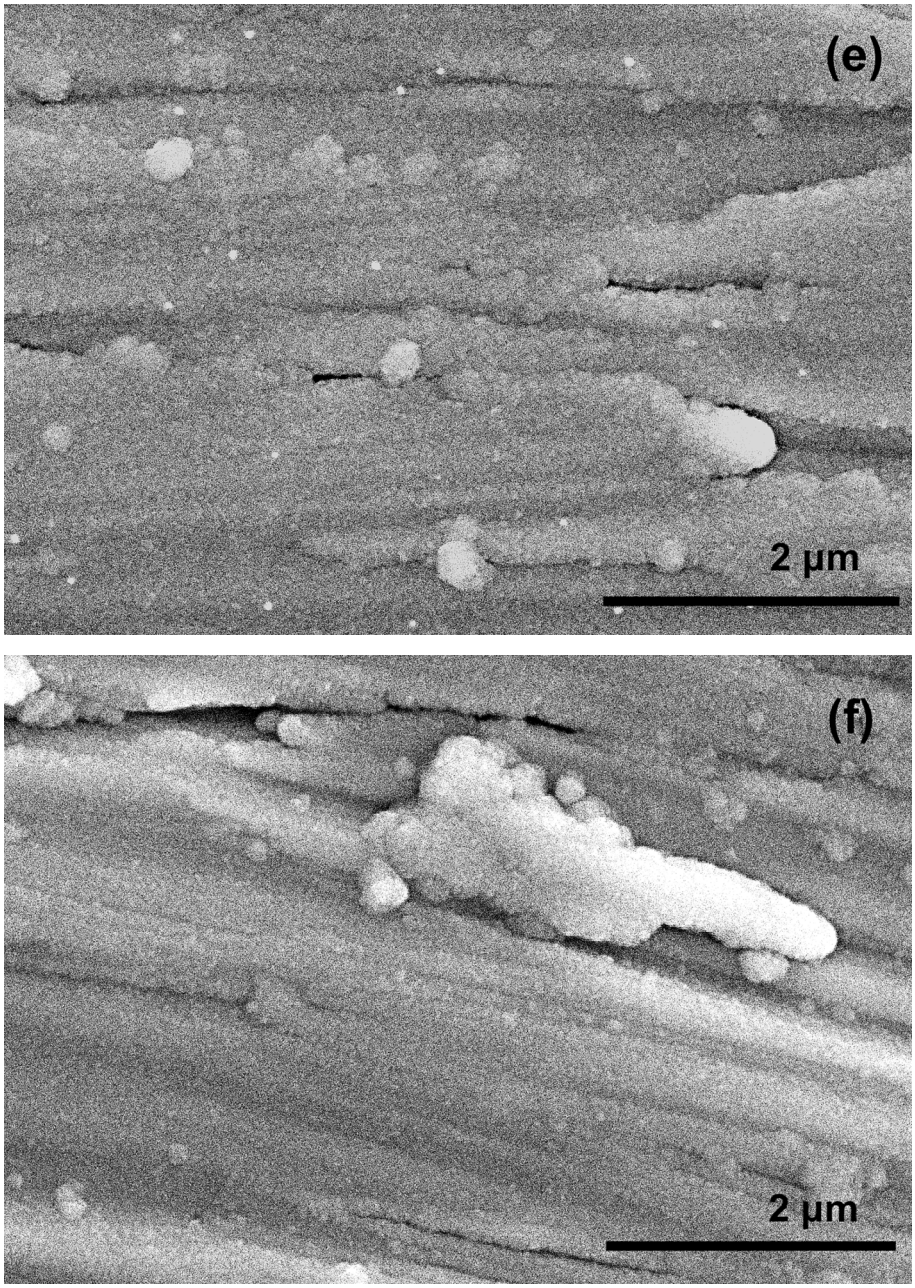

Fig. 4. (*continued*).

influence on the catalytic properties of the coatings, and the obtained values differ only within the error limits. A greater difference occurs at higher values of the current density, when the kinetics of the process is determined by diffusion: the formed oxygen bubbles into the solution and the access of new electrolyte to the surface of the catalyst. Quantitative parameters of the electrocatalytic activity of the coatings deposited by the MS method revealed the advantage of the amorphous structure, since the coatings formed in a 100 % argon atmosphere have a lower OER overpotential than the coatings obtained in the chamber after replacing part of the argon with oxygen. However, the 20 %Ar/80 %O_2 coating with higher crystallinity has the lowest Tafel constant value, suggesting slightly better reaction kinetics.

PEIS measurements at + 1.52 V as a pre-onset potential of OER were conducted to explore the resistance components of the electrocatalytical systems. Fig. 7 exhibits the Nyquist plots of investigated samples under alkaline conditions. The curves were fitted with an equivalent circuit consisting of solution resistance (R_s), a double layer capacitance (C_{dl}) and a charge transfer resistance (R_{ct}). The quantitative values of the circuit components are presented in Table 2. Impedance measurements largely support the previous CV results, which highlighted that electrochemically formed coatings have considerably lower double layer capacitance. Although reduced C_{dl} values can be advantageous for the OER since formation of oxo species on the surface might limit the charge transfer throughout the bulk active material [26], increased porosity during ED synthesis also provided a higher R_{ct}. Meanwhile, amorphous iron oxide coating (100 % Ar) has demonstrated the lowest semicircle in the Nyquist plots, resulting in the lowest R_{ct} values (8.09 Ω·cm^{-2}).

The long-term stability of an electrocatalyst is a crucial parameter describing its application at the industrial level. A study of 24-hour chronopotentiometry at 10 mA·cm^{-2} current density (Fig. S6) has disclosed a very high stability of all hematite coatings prepared during this work. All tested coatings pass through the alkaline activation process during first 5 h of oxygen formation. It was determined that samples with more expressed crystallinity, in particular hematite prepared by ED

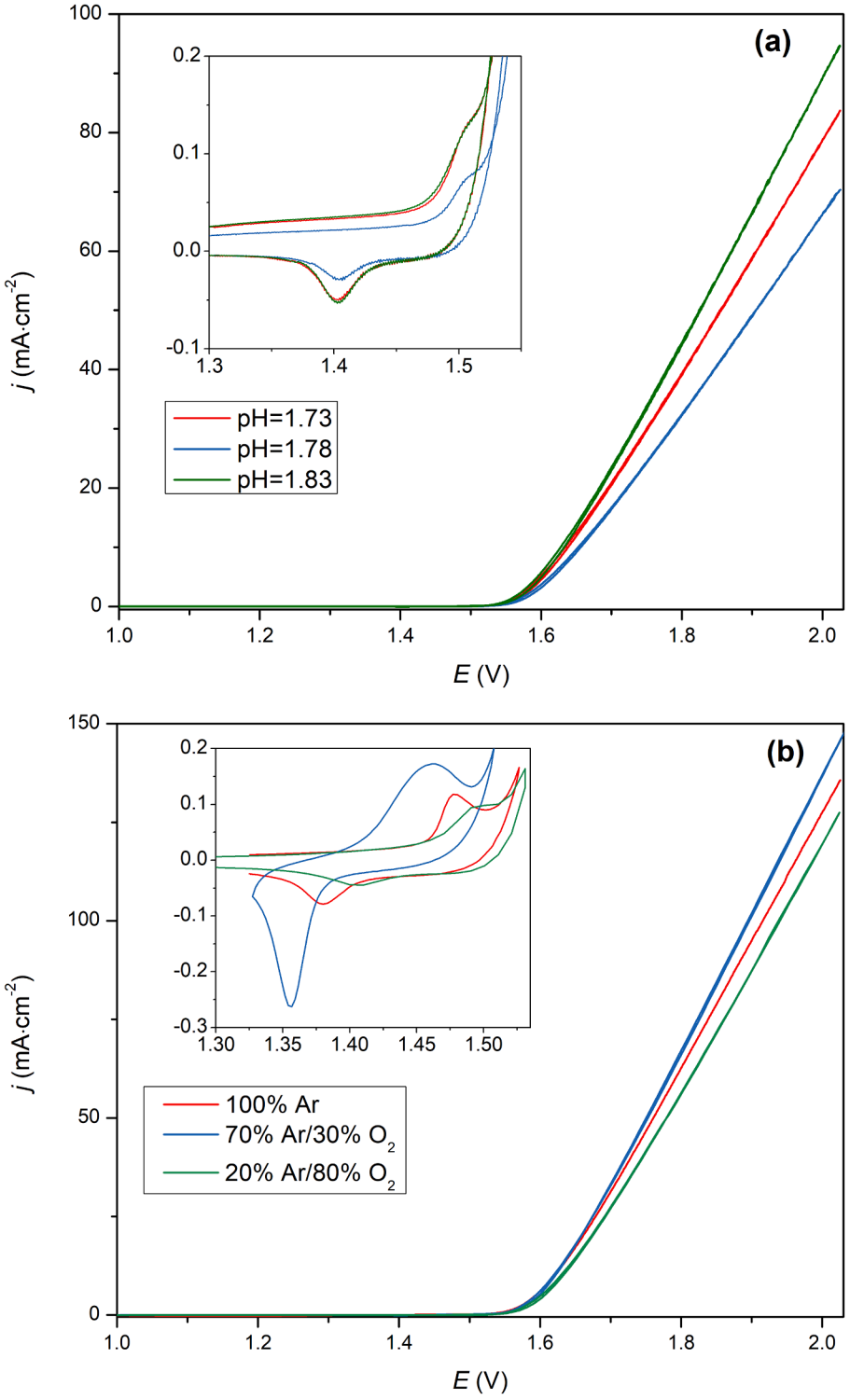

Fig. 5. (*a*) Linear sweep voltammograms of α-Fe_2O_3 coatings on AISI302 steel in 1.0 M KOH at a scan rate of 20 mV·s^{-1}. (*b*) Linear sweep voltammograms of compact hematite coatings synthesized via MS technique with different gas ratios in the chamber. Insets - cyclic voltammograms of hematite coatings at 50 mV·s^{-1} scan rate in 1.0 M KOH.

and annealed as well as crystalline coating obtained by MS in 20 %Ar/80 %O_2 atmosphere, finish their activation faster (during 5–6 h of intensive bubble formation) but maintain 99.4 % and 99.8 % of their initial potential, respectively. Meanwhile, it was noted that more amorphous coatings synthesized via MS with no or less oxygen in the deposition chamber still undergoes the activation after 24 h since their potential tends to slightly decrease by 0.33 % (100 % Ar) and 0.09 % (70 %Ar/30 %O_2).

The long-term stability of iron oxide is highly related to the corrosion processes occurring under the unfavourable alkaline conditions. The anodic corrosion is associated with oxidation processes of iron, meanwhile, the cathodic processes that can inevitably occur on the surface is related with the oxygen migration from the electrolyte to the interface of the active material where its reduction takes place forming hydroxyl

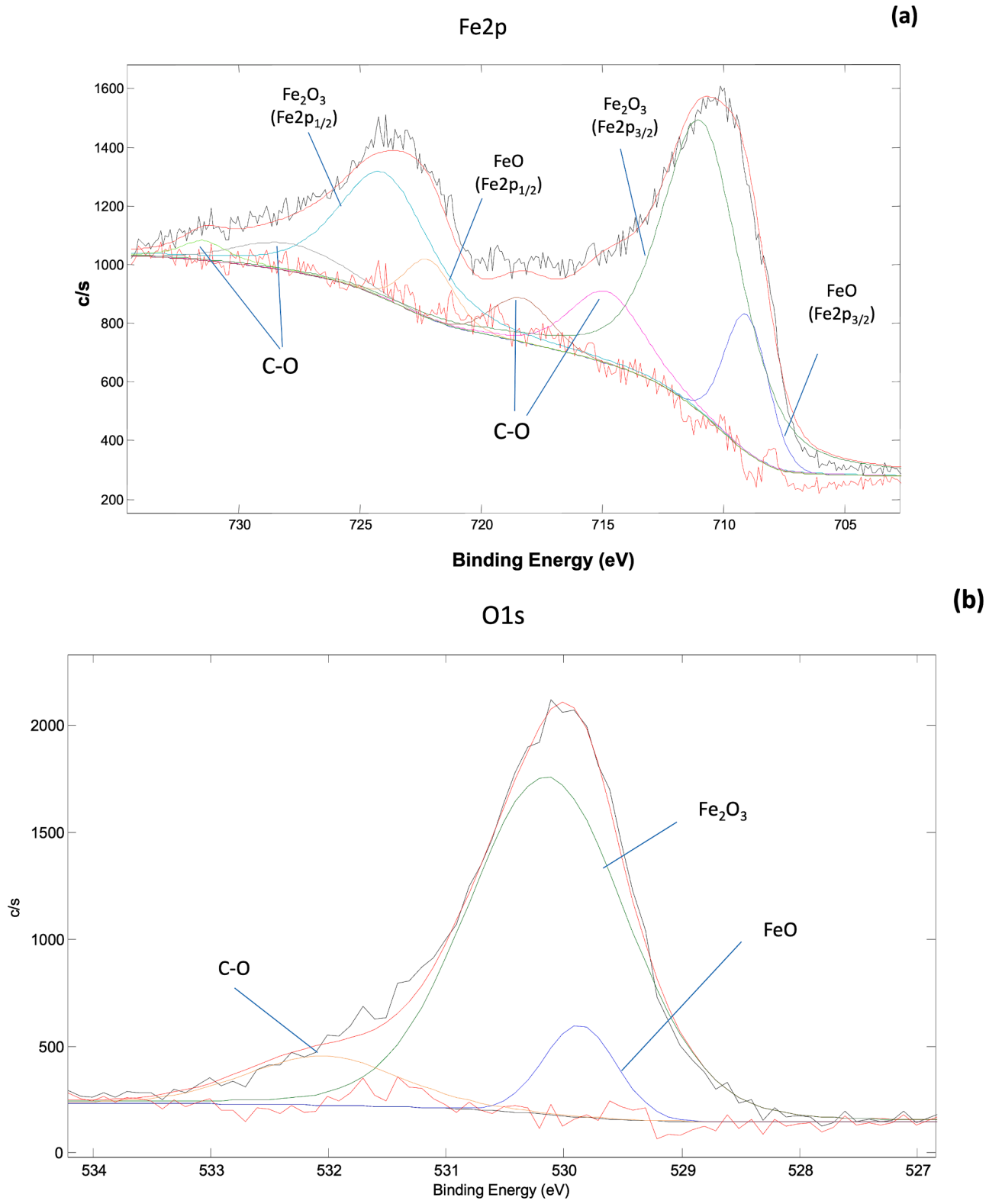

Fig. 6. Representative Fe2p (*a*) and O1s (*b*) XPS spectra of iron oxide deposited by MS in 100% Ar atmosphere.

ions [27]. The study on coatings corrosion (Fig. S7 and Table 2) has revealed that porous sample has a tendency to corrode the least of all tested samples since it presented almost 10 times smaller j_{corr} values. It might be related to its less favourable surface to form a double layer with oxo derivatives, as also reflected in C_{dl} calculations.

Finally, the behaviour of oxygen bubbles was investigated with optical microscope during the intensive oxidation of all coatings. The images taken during OER process (Fig. S8 and Video S9) have disclosed that bubbles detach from the surface without coalescence and strong adhesion to the surface. The approximate diameter of oxygen bubbles does not exceed 100 μm and correlates well with the data presented by other authors [28].

Table 1
Kinetic parameters of OER on hematite coatings prepared by ED and MS.

Iron oxide prepared by ED			
Parameter	**pH = 1.73**	**pH = 1.78**	**pH = 1.83**
Onset at OER (mV)	550	559	548
Overpotential at onset (mV)	344	353	342
Tafel slope *b* (mV·dec^{-1})	48	47	50
Iron oxide prepared by MS			
Parameter	**100 % Ar**	**70 % Ar/30 % O_2**	**20 % Ar/80 % O_2**
Onset at OER (mV)	547	554	561
Overpotential at onset (mV)	341	348	355
Tafel slope *b* (mV·dec^{-1})	59	58	51

Table 2
Electroactive surface, corrosion and impedance parameters of iron oxide coatings.

Parameter	**Electrodeposited (pH = 1.83)**	**100 % Ar**	**70 %Ar / 30 %O_2**	**20 %Ar / 80 %O_2**
C_{dl} (mF·cm^{-2})	0.0046	0.0747	0.0660	0.059
ECSA (cm^2)	1.2	3.4	3.0	2.7
E_{corr} (mV)	828	815	891	866
j_{corr} (μA·cm^{-2})	0.049	0.136	0.117	0.098
β_a (mV)	243.6	135.0	151.1	174.5
β_a (mV)	61.1	34.7	31.2	30.8
CR (μm·year^{-1})	0.49	1.55	1.53	1.12
R_s (Ω·cm^{-2})	2.56	4.65	3.86	3.34
C_{dl} (mF·cm^{-2})	0.16	0.68	1.20	0.94
R_{ct} (Ω·cm^{-2})	11.56	8.09	12.21	11.23

4. Conclusions

In this work, thin films of iron oxide were formed in two ways: i) potentiodynamic cycling was used to obtain porous morphology samples and ii) compact coatings were synthesized by magnetron sputtering. A detailed structural analysis has revealed the hematite-based structures obtained in both cases with some magnetite impurities in the case of MS synthesis. SEM images of electrodeposited coatings showed a distinctive clustering behaviour with a horizontally orientated lamellar structure. Whereas SEM micrographs of MS synthesized coatings demonstrated the compactness of the surface with agglomerates within the range of 200–600 nm. Electrocatalytic evaluation of the coatings showed that there is no significant difference with respect to the overpotential of the reaction onset potential, which is 342–353 mV for electrodeposited samples and 341–355 mV for those obtained by the MS method. However, the advantage of compact coatings emerges at higher current density values, when the activity of porous coatings is limited by diffusion from and into the pores. Calculations of the coefficient *b* of the Tafel equation, which in general shows the reaction kinetics and the possible limiting step, revealed the superiority of porous structures (avg. 48 mV·dec^{-1}) at the beginning of the reaction over compact coatings (avg. 56 mV·dec^{-1}). This difference is probably related to the larger surface area of the porous structures, which also increases the concentration of the active centres of the reaction. On summary of the obtained results, it can be assumed that porous surfaces are responsible for a higher concentration of active centres, which improves the reaction kinetics. However, at higher current density values, compact structures gain an obvious advantage, because they are less affected by the removal of the reaction product from the surface and the entry of electrolyte ions.

CRediT authorship contribution statement

Ieva Barauskienė: Writing – original draft, Visualization, Validation, Software, Resources, Methodology, Investigation, Data curation, Conceptualization. **Jean-François Blach:** Writing – review & editing,

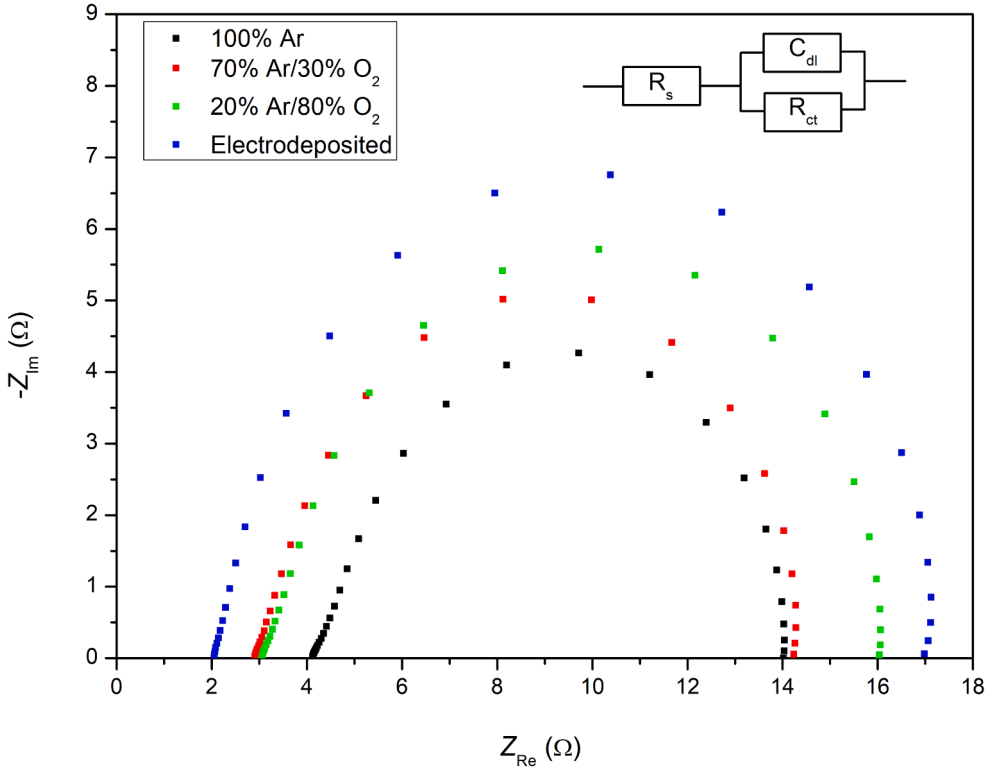

Fig. 7. Nyquist plots of iron oxide coatings prepared via MS and ED methods. The data were fitted with an equivalent circuit demonstrated on the figure: R_s+C_{dl}/R_{ct}.

Software, Methodology, Investigation, Data curation. **Sebastien Saitzek:** Writing – review & editing, Software, Methodology, Investigation, Data curation. **Jolanta Rousseau:** Writing – review & editing, Investigation. **Christian Mathieu:** Software, Methodology, Investigation, Data curation. **Vidas Pakštas:** Software, Methodology, Investigation, Data curation. **Eugenijus Valatka:** Writing – review & editing, Conceptualization. **Giedrius Laukaitis:** Writing – review & editing, Methodology, Investigation, Data curation.

Funding

This work was supported by the Research Council of Lithuania [grant number P-PD-22–129].

Declaration of competing interest

The authors declare that they have no known competing financial interests or personal relationships that could have appeared to influence the work reported in this paper.

Acknowledgments

“Ministère de l’Enseignement Supérieur et de la Recherche”, “Région Hauts-de-France” and “FEDER” are thanked for supporting and funding this work notably through the CPER Manifest program.

Appendix A. Supplementary data

Supplementary data to this article can be found online at https://doi.org/10.1016/j.apsusc.2025.162576.

Data availability

No data was used for the research described in the article.

References

[1] Communication from the Commission to the European Parliament, the Council, the European Economic and Social Commitee and the Commitee of the Regions. A hydrogen strategy for a climate-neutral Europe, 2021. https://eur-lex.europa.eu/legal-content/EN/TXT/HTML/?uri=CELEX:52020DC0301 (accessed 8 October 2024).

[2] Net zero by 2050. A roadmap for the global energy sector, 2021. https://iea.blob.core.windows.net/assets/deebef5d-0c34-4539-9d0c-10b13d840027/NetZeroby2050-ARoadmapfortheGlobalEnergySector_CORR.pdf (accessed 8 October 2024).

[3] C. Hu, L. Zhang, J. Gong, Recent progress made in the mechanism comprehension and design of electrocatalysts for alkaline water splitting, Energy Environ. Sci. 12 (2019) 2620–2645, https://doi.org/10.1039/c9ee01202h.

[4] H.A. Miller, K. Bouzek, J. Hnat, S. Loos, C.I. Bernäcker, T. Weißgärber, L. Röntzsch, J. Meier-Haack, Green hydrogen from anion exchange membrane water electrolysis: a review of recent developments in critical materials and operating conditions, Sustainable, Energy Fuels 4 (2020) 2114–2133, https://doi.org/10.1039/C9SE01240K.

[5] C. Santoro, A. Lavacchi, P. Mustarelli, V. Di Noto, L. Elbaz, D.R. Dekel, F. Jaouen, What is Next in Anion-Exchange Membrane Water Electrolyzers? Bottlenecks, Benefits, and Future, ChemSusChem 15 (2022), https://doi.org/10.1002/cssc.202200027.

[6] I.T. Cousins, G. Goldenman, D. Herzke, R. Lohmann, M. Miller, C.A. Ng, S. Patton, M. Scheringer, X. Trier, L. Vierke, Z. Wang, J.C. DeWitt, The concept of essential use for determining when uses of PFASs can be phased out, Environ. Sci.: Processes Impacts 21 (2019) 1803–1815, https://doi.org/10.1039/c9em00163h.

[7] Y. Zhang, Q. Fu, B. Song, P. Xu, Regulation Strategy of Transition Metal Oxide-Based Electrocatalysts for Enhanced Oxygen Evolution Reaction, Acc. Mater. Res. 3 (2022) 1088–1100, https://doi.org/10.1021/accountsmr.2c00161.

[8] Q. Zhao, Z. Yan, C. Chen, J. Chen, Spinels: Controlled Preparation, Oxygen Reduction/Evolution Reaction Application, and Beyond, Chem. Rev. 117 (2017) 10121–10211, https://doi.org/10.1021/acs.chemrev.7b00051.

[9] H. Li, X. Han, W. Zhao, A. Azhar, S. Jeong, D. Jeong, J. Na, S. Wang, J. Yu, Y. Yamauchi, Electrochemical preparation of nano/micron structure transition metal-based catalysts for the oxygen evolution reaction, Mater. Horiz. 9 (2022) 1788–1824, https://doi.org/10.1039/D2MH00075J.

[10] Q.-Q. Xu, W. Huo, S.-S. Li, J.-H. Fang, L. Li, B.-Y. Zhang, F. Zhang, Y.-X. Zhang, S.-W. Li, Crystal phase determined Fe active sites on Fe_2O_3 (γ- and α-Fe_2O_3) yolk-shell microspheres and their phase dependent electrocatalytic oxygen evolution reaction, Appl. Surf. Sci. 533 (2020) 147368, https://doi.org/10.1016/j.apsusc.2020.147368.

[11] R.R. Raja Sulaiman, W.Y. Wong, K.S. Loh, Recent developments on transition metal–based electrocatalysts for application in anion exchange membrane water electrolysis, Int. J. Energy Res. 46 (2022) 2241–2276, https://doi.org/10.1002/er.7380.

[12] R.B. Espinosa, M.H.G. Duits, D. Wijnperle, F. Mugele, L. Lefferts, Bubble formation in catalyst pores; curse or blessing?, React, Chem. Eng. 3 (2018) 826–833, https://doi.org/10.1039/c8re00110c.

[13] W.-J. Zhou, D.-D. Zhao, M.-W. Xu, C.-L. Xu, H.-L. Li, Effects of the electrodeposition potential and temperature on the electrochemical capacitance behavior of ordered mesoporous cobalt hydroxide films, Electrochim. Acta 53 (2008) 7210–7219, https://doi.org/10.1016/j.electacta.2008.05.007.

[14] E. López-Fernández, C. Gómez-Sacedón, J. Gil-Rostra, J.P. Espinós, A.R. González-Elipe, F. Yubero, A. de Lucas-Consuegra, Ionomer-Free Nickel-Iron bimetallic electrodes for efficient anion exchange membrane water electrolysis, Chem. Eng. J. 433 (2022) 133774, https://doi.org/10.1016/j.cej.2021.133774.

[15] H. Schäfer, M. Chatenet, Steel: The Resurrection of a Forgotten Water-Splitting Catalyst, ACS Energy Lett. 3 (2018) 574–591, https://doi.org/10.1021/acsenergylett.8b00024.

[16] E. Gileadi, E. Kirowa-Eisner, Some observations concerning the Tafel equation and its relevance to charge transfer in corrosion, Corros. Sci. 47 (2005) 3068–3085, https://doi.org/10.1016/j.corsci.2005.05.044.

[17] J.R.H. Ross, Chapter 5 - Catalyst Characterization, in: J.R.H. Ross (Ed.), Contemporary Catalysis. Fundamentals and Current Applications, Elsevier, Amsterdam, 2019, pp. 121–132. Doi: Doi: 10.1016/B978-0-444-63474-0.00005-9.

[18] G.H.A. Therese, P.V. Kamath, Electrochemical Synthesis of Metal Oxides and Hydroxides, Chem. Mater. 12 (2000) 1195–1204, https://doi.org/10.1021/cm990447a.

[19] J.R.S. Brownson, C. Lévy-Clément, Nanostructured α- and β-cobalt hydroxide thin films, Electrochim. Acta 54 (2009) 6637–6644, https://doi.org/10.1016/j.electacta.2009.06.034.

[20] V. Goossens, J. Wielant, S. Van Gils, R. Finsy, H. Terryn, Optical properties of thin iron oxide films on steel, Surf. Interface Anal. 38 (2006) 489–493, https://doi.org/10.1002/sia.2219.

[21] S.-H. Shim, T.S. Duffy, Raman spectroscopy of Fe_2O_3 to 62 GPa, Am. Mineral. 87 (2002) 318–326, https://doi.org/10.2138/am-2002-2-314.

[22] T. Szatkowski, M. Wysokowski, G. Lota, D. Pęziak, V.V. Bazhenov, G. Nowaczyk, J. Walter, S.L. Molodtsov, H. Stöcker, C. Himcinschi, I. Petrenko, A.L. Stelling, S. Jurga, T. Jesionowski, H. Ehrlich, Novel nanostructured hematite–spongin composite developed using an extreme biomimetic approach, RSC Adv. 5 (2015) 79031–79040, https://doi.org/10.1039/C5RA09379A.

[23] S. Anantharaj, P.E. Karthik, S. Noda, The Significance of Properly Reporting Turnover Frequency in Electrocatalysis Research, Angew. Chemie Int. Ed. 60 (2021) 23051–23067, https://doi.org/10.1002/anie.202110352.

[24] G. Li, L. Anderson, Y. Chen, M. Pan, P.-Y.-A. Chuang, New insights into evaluating catalyst activity and stability for oxygen evolution reactions in alkaline media, Sustain, Energy Fuels 2 (2018) 237–251, https://doi.org/10.1039/c7se00337d.

[25] N. Esfandiari, M. Aliofkhazraei, A.N. Colli, F.C. Walsh, S. Cherevko, L.A. Kibler, M. M. Elnagar, P.D. Lund, D. Zhang, S. Omanovic, J. Lee, Metal-based cathodes for hydrogen production by alkaline water electrolysis: Review of materials, degradation mechanism, and durability tests, Prog Mater Sci 144 (2024) 101254, https://doi.org/10.1016/j.pmatsci.2024.101254.

[26] H. Liang, M. Xu, E. Asselin, Corrosion of monometallic iron- and nickel-based electrocatalysts for the alkaline oxygen evolution reaction: A review, J Power Sources 510 (2021) 230387, https://doi.org/10.1016/j.jpowsour.2021.230387.

[27] X. Chen, X.G. Li, C.W. Du, Y.F. Cheng, Effect of cathodic protection on corrosion of pipeline steel under disbonded coating, Corros Sci 51 (2009) 2242–2245, https://doi.org/10.1016/j.corsci.2009.05.027.

[28] J. Kim, A.P. Tiwari, C. Qin, T.G. Novak, J. Lee, J. Kim, M. Park, J.-K. Kim, S. Jeon, Enhanced Oxygen Evolution Reaction by Efficient Bubble Dynamics of Aligned Nonoxidized Graphene Aerogels, ACS Sustain Chem Eng 9 (2021) 10326–10334, https://doi.org/10.1021/acssuschemeng.1c03285.